

Black hole mergers: the first light

Elena M. Rossi¹, G. Lodato^{2,3}, P. J. Armitage^{4,5}, J. E. Pringle^{6,3} and A. R. King³

¹*Racah Institute of Physics, The Hebrew University, Jerusalem 91904, Israel*

²*Università degli Studi di Milano, Dipartimento di Fisica, via Celoria 16, I-20133 Milano, Italy*

³*Department of Physics and Astronomy, University of Leicester, Leicester, LE1 7RH, UK*

⁴*JILA, 440 UCB, University of Colorado, Boulder, CO 80309-0440, USA*

⁵*Department of Astrophysical and Planetary Sciences, University of Colorado, Boulder, USA*

⁶*Institute of Astronomy, Madingley Road, Cambridge, CB3 0HA, UK*

e-mail: emr@phys.huji.ac.il (EMR)

31 October 2018

ABSTRACT

The coalescence of supermassive black hole binaries occurs via the emission of gravitational waves, that can impart a substantial recoil to the merged black hole. We consider the energy dissipation, that results if the recoiling black hole is surrounded by a thin circumbinary disc. Our results differ significantly from those of previous investigations. We show analytically that the dominant source of energy is often potential energy, released as gas in the outer disc attempts to circularize at smaller radii. Thus, dimensional estimates, that include only the kinetic energy gained by the disc gas, underestimate the real energy loss. This underestimate can exceed an order of magnitude, if the recoil is directed close to the disc plane. We use three dimensional Smooth Particle Hydrodynamics (SPH) simulations and two dimensional finite difference simulations to verify our analytic estimates. We also compute the bolometric light curve, which is found to vary strongly depending upon the kick angle. A prompt emission signature due to this mechanism may be observable for low mass ($10^6 M_{\odot}$) black holes whose recoil velocities exceed $\sim 10^3 \text{ km s}^{-1}$. Emission at earlier times can mainly result from the response of the disc to the loss of mass, as the black holes merge. We derive analytically the condition for this to happen.

Key words: black hole physics — accretion, accretion discs — hydrodynamics

1 INTRODUCTION

Supermassive black hole binaries are predicted by hierarchical galaxy formation models and are a likely consequence of observed galaxy mergers. However, only a handful of these binaries have been directly observed (Rodriguez et al. 2006) and their dynamical evolution is still uncertain. If binaries coalesce on a time-scale shorter than the age of the universe, mergers can be an important ingredient in the evolution and growth of supermassive black holes. Mergers also emit low frequency gravitational waves whose detection is one of the prime goals of proposed experiments such as the *Laser Interferometer Space Antenna* (LISA). What remains uncertain is whether detectable electromagnetic emission occurs either prior to or in the immediate aftermath of the coalescence.

Observations and numerical simulations strongly suggest that mergers of gas-rich galaxies result in the inflow of gas into the nuclear region, where it is likely to co-exist with a newly formed black hole binary (Escala et al. 2005; Dotti et al. 2007; Callegari et al. 2009). The gas may have an active role and mediate and speed up the coalescence (Ivanov et al. 1999; Armitage & Natarajan 2002; Cuadra et al. 2009; Lodato et al. 2009). However – and irrespective of whether the gas is *dynamically* important – if gas is present then perturbations to the gas during the merger may give rise to

observable electromagnetic signals that can either precede or follow the gravitational wave signal. Observations of these signals can give us evidence for the existence of mergers, improve upon LISA’s limited ability to spatially localise sources, and teach us about the astrophysical phenomena involved in the process.

General relativity predicts that gravitational waves emitted by the shrinking binary during the final coalescence carry away a non-zero net linear momentum, so that the centre of mass of the merged black holes recoils (Peres 1962; Miller et al. 2007). A number of authors have used semi-analytic methods or N-body simulations to estimate the influence of the recoil on a surrounding thin disc (Lippai et al. 2008; Shields & Bonning 2008; Schnittman & Krolik 2008). Hydrodynamic simulations for a thick disc – a configuration that we do not consider here – have also been performed by Megevand et al. (2009).

Here we revisit the analytic problem (emphasizing the importance of different physical effects from those discussed previously), and perform numerical simulations to investigate how a thin, non self-gravitating disc reacts to the birth of a central black hole via merger. The initial disc geometry that we consider is based upon that discussed by Armitage & Natarajan (2002) and Milosavljević & Phinney (2005). We assume that, at a time signif-

icantly prior to the final coalescence (when the binary semi-major axis was $> 10^2$ Schwarzschild radii), the binary was surrounded by a geometrically thin disc whose plane coincided with that of the binary. While the binary remains in tidal contact with this disc, energy and angular momentum can be exchanged between the two. This exchange provides an additional source of heat for the inner disc (Lodato et al. 2009), and alters its long term viscous evolution (Pringle 1991). Immediately prior to the coalescence, however, the rapid decay of the binary orbit due to gravitational wave emission leads to a decoupling of the binary from the inner disc. As a result, it is a reasonable first approximation to model the effect of a kick on an initially unperturbed, axisymmetric circumbinary disc. We also ignore any effects associated with gas that has survived in circumpriary or circumssecondary discs up until near the moment of coalescence. Such gas, if present, may produce observable signatures (Armitage & Natarajan 2002; Lodato et al. 2009; Chang et al. 2009), but it is decoupled dynamically from the gas in the circumbinary disc. The effect of the recoil on the circumbinary disc can therefore be considered independently from the fate of gas bound to either of the individual black holes.

In this paper, our main focus is on the effect of the black hole recoil rather than the almost instantaneous mass loss that also accompanies the merger (Milosavljević & Phinney 2005). We study the consequence of velocity perturbations in both the linear (kick velocity smaller than circular velocity) and non linear regimes. We calculate the magnitude of energy dissipation and assess the dependence of this potentially observable quantity on the recoil geometry. In particular, we focus on off-plane kicks, which are expected to be the most common.

The paper is organised as follows. In Section 2 we analytically investigate the properties of the disc after the kick and the dissipation of the extra energy in the innermost region. These estimates serve as guidance for our numerical simulations, described in Section 3. In Section 4 we present our numerical results, which we discuss in Section 5. Finally, in Section 6 we draw our conclusions.

2 ANALYTIC ESTIMATES

2.1 Disc topology: bound and unbound regions

We first consider the reaction to the kick of particles at radius R . Initially, the particles rotate anti-clockwise around the black hole in circular orbits with Keplerian velocity $\mathbf{V}_k = \sqrt{GM/R} \hat{\phi}$, where ϕ is the angle between the positive y -axis and the particle radius R , M is the mass of the merged black hole and G is the gravitational constant (see Fig. 1). The angular velocity is $\Omega = \sqrt{GM/R^3}$.

In the frame of the moving central object the recoil results in each particle receiving an additional velocity \mathbf{V} . The kick velocity direction makes an angle θ with the disc plane. For simplicity, we assume that the projection onto the disc plane, $V \cos \theta$, is in the direction of the positive x -axis (see Fig. 1). In cylindrical coordinates the three components of the initial particle velocity are then $V_R = -V \cos \theta \sin \phi$, $V_\phi = V_k - V \cos \theta \cos \phi$ and $V_z = V \sin \theta$.

If the disc extends to sufficiently large radii, there is a radius R_v at which $V = V_k$. In the following, it is convenient to adopt the dimensionless radial coordinate $r = R/R_v = (V/V_k)^2$. The specific energy of a particle then reads

$$\epsilon = -\frac{1}{2}V_k^2(1 + 2\sqrt{r}\cos\theta\cos\phi - r). \quad (1)$$

A particle can escape from the system ($\epsilon > 0$) or it can remain bound to it ($\epsilon < 0$), depending on its distance from the hole and on

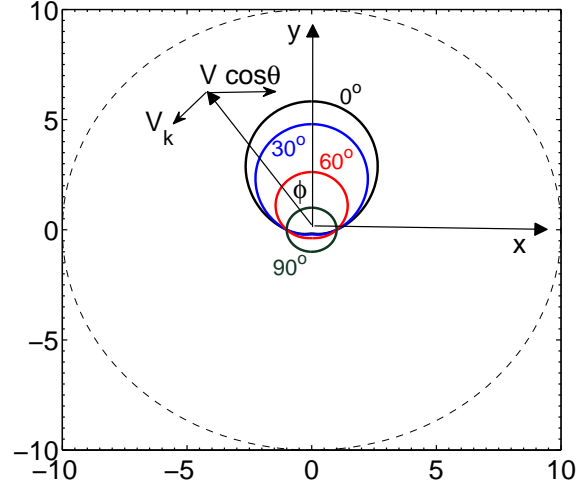


Figure 1. Face-on view of the disc showing the the Keplerian velocity V_k and the projection of the kick velocity onto the disc plane $V \cos \theta$. The angle between the positive y -axis and the particle's position is ϕ . The closed solid lines mark the border between the bound and unbound regions for kick angles between 0° (a kick directed into the disc plane) and 90° . As θ approaches 90 degrees, the bound region becomes increasingly azimuthally symmetric.

the direction of the kick velocity relative to its original Keplerian velocity. In particular at small radii,

$$r < r_b = (-\cos \theta + \sqrt{\cos^2 \theta + 1})^2, \quad (2)$$

all particles within a given annulus are bound, while for

$$r > r_{ub} = (\cos \theta + \sqrt{\cos^2 \theta + 1})^2, \quad (3)$$

all particles are unbound. The dimensionless radii $r_b = R_b/R_v$ and $r_{ub} = R_{ub}/R_v$ correspond to the actual radii R_b and R_{ub} , respectively. In the radial range between r_b and r_{ub} , particles at radius r are bound only within a limited azimuthal range $-\phi_b < \phi < \phi_b$ (with $0 \leq \phi_b \leq \pi$), where

$$\cos \phi_b = \frac{r - 1}{2\sqrt{r}\cos\theta}. \quad (4)$$

In Fig. 1 we show the boundaries of the bound region for different kick angles. As θ increases, the bound region becomes increasingly azimuthally symmetric, while the radial extent of the bound region between r_b and r_{ub} decreases. For a perpendicular kick $r_b = r_{ub} = 1$.

In our analytic estimates we consider only the portion of the disc that is still bound after the kick, since matter that is unbound by the recoil simply leaves the system and it is not energetically important.

2.2 Angular momentum

In the bound portion of the disc (where $\epsilon < 0$), particles are excited on elliptical orbits with eccentricity $e^2 = 1 + 2j^2\epsilon/(GM)^2$, and with specific angular momentum

$$\frac{\mathbf{j}}{J_k} = (1 - \sqrt{r}\cos\theta\cos\phi)\hat{z} - \sqrt{r}\sin\theta\hat{\phi}, \quad (5)$$

where $J_k = RV_k$ is the Keplerian specific angular momentum for that radius. In general $\mathbf{j} \neq \mathbf{J}_k$, and as a consequence rearrangement

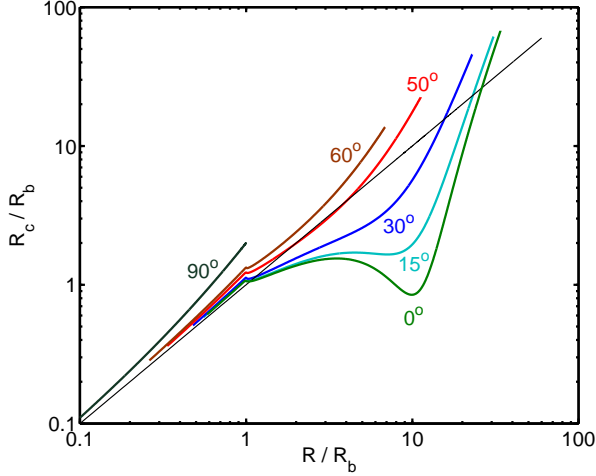


Figure 2. The mean circularisation radius (equation 7) in units of R_b (equation 2) as a function of the initial location R in the same units. The black solid thin line ($R = R_c$) divides the region where outward spreading occurs (upper part $R_c > R$) from the region where accretion occurs ($R_c < R$).

of gas must occur after the recoil as the gas seeks a new minimum energy configuration. If a particle conserves its angular momentum then it must circularize at a radius $r_{c,p} = R_{c,p}/R_V$ given by

$$\frac{r_{c,p}}{r} = \left(\frac{j}{J_k}\right)^2 = (1 - \sqrt{r} \cos \theta \cos \phi)^2 + r \sin^2 \theta. \quad (6)$$

To understand the behaviour of the disc after the kick, we calculate the mean circularization radius for a ring, $r_c = R_c/R_V$,

$$\begin{aligned} \frac{r_c}{r} &= \frac{1}{2\phi_b} \int_{-\phi_b}^{\phi_b} \left(\frac{j}{J_k}\right)^2 d\phi = (1 + r \sin^2 \theta) + \\ &r \cos^2 \theta \left(\frac{1}{2} + \frac{\sin 2\phi_b}{2\phi_b}\right) - 2\sqrt{r} \cos \theta \frac{\sin \phi_b}{\phi_b}, \end{aligned} \quad (7)$$

where the integration limits are such that $\phi_b = \pi$, for $r \leq R_b$. Fig. 2 shows that while matter at $R < R_b$ circularizes close to its original location for any kick angle, R_c depends strongly on the kick angle for $R > R_b$. For high latitude kicks ($\theta \gtrsim 50^\circ$), the behaviour outside and inside R_b is similar. For smaller inclination angles an increasing amount of matter circularizes at smaller radii, and only a small fraction of matter expands toward larger radii. This implies that there must be a net release of potential energy.

For out-of-the plane kicks, the recoiling matter acquires in general an *azimuthal* component in its new angular momentum (equation 5). Its magnitude varies with radius, so we expect the disc to be warped initially. After the extra energy associated with the warp is dissipated, the disc must lie in a plane, however tilted with respect to its original orientation.

2.3 Energy dissipation

In the previous section, we showed that particles that remain bound after the kick do not, in general, have the same specific angular momentum as they had prior to the kick. Initially their orbits are eccentric. In a fluid disc, orbit crossing leads to energy dissipation and circularization of the disc into a new circular equilibrium configuration.

We estimate the total energy available for dissipation by assuming that each particle that remains bound circularizes at the radius appropriate to its post-kick angular momentum. We write this as,

$$E_{\text{diss}} = E - E_c, \quad (8)$$

where E is the initial post-kick energy of the bound disc (including the gain or loss of kinetic energy resulting from the kick) and E_c is its energy after circularization. The initial energy is obtained by integrating the specific energy (equation 1) over the bound region of the disc,

$$E = \int_{R_{\text{in}}}^{R_{\text{ub}}} \int_{-\phi_b}^{\phi_b} \epsilon \Sigma R dR d\phi. \quad (9)$$

Here Σ is the disc surface density, R_{in} is the inner radius of the disc, and it is to be understood that the limits on the angular integral are such that $\phi_b = \pi$ when $R \leq R_b$.

After circularization the total energy of the gas within the disc is

$$E_c = \int_{R_{\text{in}}}^{R_{\text{ub}}} \int_{-\phi_b}^{\phi_b} -\frac{1}{2} V_k^2 \left(\frac{r}{r_{c,p}}\right) \Sigma R dR d\phi, \quad (10)$$

where $(r/r_{c,p})$ is given by equation (6). The integral over ϕ is analytic and can readily be evaluated using a symbolic algebra package. However the simplest general form we have found is extremely lengthy, and we do not write it here.

To assess which parts of the disc contribute the most to E_{diss} we now specialize to a disc with a power-law surface density profile $\Sigma = \Sigma_V r^{-p}$, where $\Sigma_V = \Sigma(r=1)$. Dimensional arguments¹ suggest that the change in kinetic energy is of the order of $(V^2/2)\Sigma_V R_V^2$. Hence we write the differential contribution to the total energy release as,

$$\frac{dE_{\text{diss}}}{dr} = \frac{V^2}{2} \Sigma_V R_V^2 g(r), \quad (11)$$

where,

$$g(r) = 2\phi_b r^{-p} \left[r - 2\sqrt{r} \cos \theta \frac{\sin \phi_b}{\phi_b} - 1 + I(r) \right], \quad (12)$$

$$I(r) = \frac{1}{2\phi_b} \int_{-\phi_b}^{\phi_b} \left(\frac{j}{J_k}\right)^{-2} d\phi. \quad (13)$$

The function $g(r)$ is a measure of how well the simple estimate $(1/2)V^2\Sigma_V R_V^2$ captures the expected total energy release. This function is plotted for different values of the kick angle (and $p = 1.5$) in Fig. 3. As θ decreases, the behaviour around $r = 1$ is increasingly dominated by I and it develops a sharp peak at $r = 1$. For $\theta = 0^\circ$, the right-hand side of equation (11) diverges as $|r - 1|^{-1}$. For $\theta \neq 0^\circ$ we integrate over radius to obtain the final estimate of E_{diss} . The dependence of E_{diss} on kick angle is shown in Fig. 4. We find that regardless of the surface density distribution, E_{diss} is almost 3 orders of magnitude larger for a kick close to the disc plane than for a perpendicular kick. Moreover the assumption made in previous papers that $(1/2)V^2\Sigma_V R_V^2$ would fairly measure E_{diss} proves to be a substantial underestimate of the energy released for all kick angles $\theta < 50^\circ$.

¹ For example, Schnittman & Krolik (2008) estimate the total energy release to be $\approx 4(V^2/2)\Sigma_V R_V^2$.

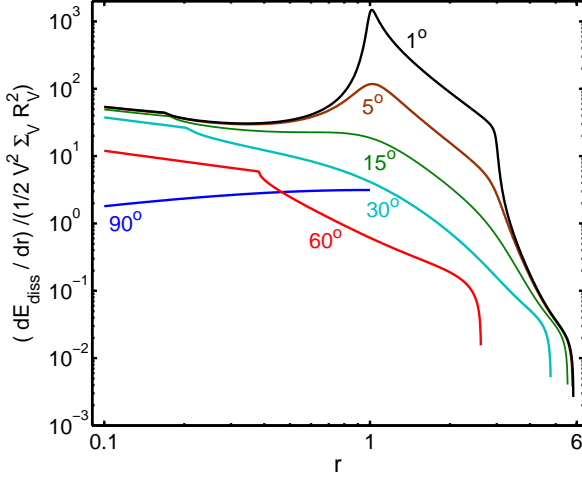


Figure 3. Differential energy to be dissipated is plotted as a function of radius (equation 11). The energy is expressed in units of $(1/2)V^2\Sigma_V R_V^2$, while the radius is in units of R_V . Different curves correspond to different kick angles as labelled. The surface density profile is $\Sigma \propto r^{-3/2}$.

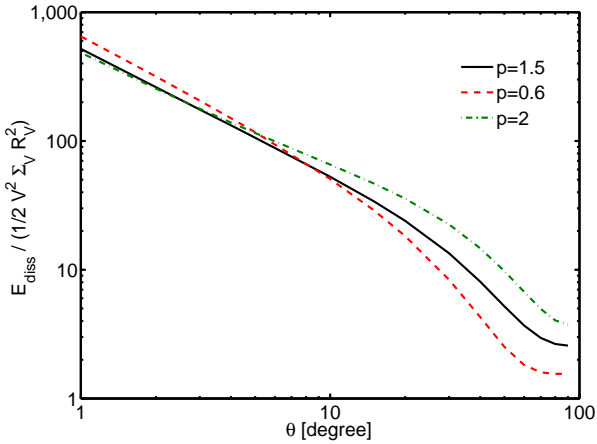


Figure 4. Total energy available to be released (equation 8) is plotted as a function of the kick angle for different power-law indexes for the surface density distribution. The energy is expressed in units of $(1/2)V^2\Sigma_V R_V^2$.

2.4 Contributions to E_{diss}

The energy available as the disc adjusts to a new equilibrium configuration can be considered to have two sources. First, there is an immediate change to the kinetic energy of particles because of the recoil. When integrated over the bound region the total energy change from this effect is positive for $\theta > 4^\circ$. Second, there is the release of potential energy that is liberated when gas in the disc loses angular momentum and circularizes at smaller radii. In the remainder of the paper we will refer to the release of potential energy on a short time scale as “accretion energy”. This should not be confused with the (much slower) energy release due to viscous disc accretion (described as “accretion energy” by Schnittman & Krolik 2008), which we do not model.

To quantify how the relative importance of the two energy sources varies with radius and with kick angle we rewrite the post-kick specific energy as

$$\epsilon = -\frac{1}{2} V_k^2 - \frac{1}{2} V_k^2 (2\sqrt{r} \cos \theta \cos \phi - r) = -\frac{1}{2} V_k^2 + \epsilon_{\text{kick}}, \quad (14)$$

and define the prompt change to the energy of the disc as,

$$E_{\text{kick}} = \int_{R_{\text{in}}}^{R_{\text{ub}}} \int_{-\phi_b}^{\phi_b} \epsilon_{\text{kick}} \Sigma R dR d\phi. \quad (15)$$

We note immediately that if $\theta = 90^\circ$ then ϵ_{kick} is simply equal to $V^2/2$. Integration over the bound region of the disc then yields $E_{\text{kick}} = (1/2)M_{\text{disc}}V^2$, where M_{disc} is the total mass within the bound region.

For arbitrary kick angles one can readily show that the contribution to E_{kick} for $R \leq R_b$ is given by the same expression,

$$\Delta E_{\text{kick}} = \frac{1}{2} \Delta M_{\text{disc}} V^2, \quad (16)$$

but where ΔM_{disc} is now the mass within the radius where the entire annulus remains bound to the hole. At larger radii, however, this is no longer true. For $R_b < R < R_{\text{ub}}$ the differential contribution to the prompt energy change dE_{kick}/dR can be either positive or negative, depending upon the radius and upon the specific kick angle. This is illustrated in Fig. 5 for the case of a kick at $\theta = 30^\circ$. When the integration is extended across the entirety of the bound disc the result is that $E_{\text{kick}} \neq (1/2)M_{\text{disc}}V^2$ for $\theta \neq 90^\circ$.

Finally we can compare the relative importance of the prompt kinetic energy to the part of E_{diss} that arises from potential energy release. In general, we find that for $R > R_b$ the gain in kinetic energy is either negative or (when positive) negligible compared to the accretion energy, whereas for $R \leq R_b$ it can be substantial (Fig. 5). As we will discuss subsequently the physical size of R_b is often quite large, so for a small disc that does not extend out to R_b it may be a reasonable approximation to assume that the disc receives an injection of kinetic energy that is subsequently dissipated. For a large disc, on the other hand, any kick that is not nearly perpendicular to the disc plane produces a wholesale rearrangement of the gas. The total energy dissipation in this regime is dominated by accretion energy, and detailed hydrodynamic simulations are needed to assess accurately the magnitude and time scale of energy release.

When we consider the energies integrated over the whole bound disc, we find that as θ decreases the fraction of E_{diss} that is due to release of potential energy increases. This is because the recoil creates larger gradients in the specific energy and angular momentum of the particles. Two effects result. First, the region between r_b and r_{ub} grows and, second, within that region more particles have a new lower specific angular momentum (see Fig. 2). Therefore, hydrodynamic simulations are needed, especially, for kicks grazing the plane and above all, for in-plane kicks, where the analytic estimate of E_{diss} fails.

2.5 Effect of mass variation of the post-remnant black hole

Not only momentum, but also energy is carried away by the gravitational waves that cause the final merger of a black hole binary. This results in a net mass loss for the system and the final black hole born by merger has a smaller mass than the sum of the masses of the two progenitors. This instantaneous mass loss of the central attractor has an effect on the surrounding gas (Milosavljević & Phinney 2005; Schnittman & Krolik 2008; O’Neill et al. 2009; Megevand et al. 2009). We show here that this effect deposits substantial energy *only* within the innermost $\sim 10^3$ Schwarzschild radii for $V > 100 \text{ km s}^{-1}$.

The argument is as follows. We first estimate the energy dissipated in the gas as the disc recovers a circular equilibrium con-

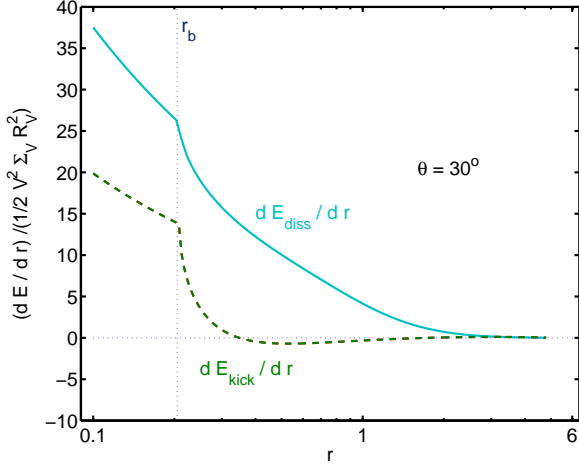


Figure 5. Differential energy available for dissipation (solid line) and change in total kinetic energy imparted directly by the kick (dashed line) is plotted as a function of radius, for $\theta = 30^\circ$. As previously, energy is in units of $(1/2)V^2\Sigma_V R_V^2$, the radius is in units of R_V , and $\Sigma \propto r^{-3/2}$.

figuration around a lighter central object, neglecting the effect of recoil. The effect of the mass loss δM is to put particles in eccentric orbits, since it instantaneously decreases their binding energy. The new specific energy of a ring initially at radius R is $\epsilon_i = -GM/(2R)(1 - 2\delta M/M)$. In the circularization process, the particles settle on a circular orbit at a *larger* radius R_c , given by angular momentum conservation: $R_c = R/(1 - \delta M/M)$. At this final radius the specific energy is $\epsilon_f = -GM/(2R)(1 - \delta M/M)^2$. Thus, the induced epicyclic motions dissipate an energy

$$\Delta\epsilon_m = \epsilon_i - \epsilon_f = \frac{1}{2}V_k^2 \left(\frac{\delta M}{M}\right)^2. \quad (17)$$

We now assess the relative importance at a given radius of the effects of the mass loss compared to that of the recoil. Equation (17) shows that $\Delta\epsilon_m \propto R^{-1}$ is a decreasing function of radius. Since the contribution of mass loss turns out to be important only within R_b , we can compare $\Delta\epsilon_m$ with the energy imparted by the recoil $\approx V^2/2$. We find that there is a radius $R_m < R_b$ *within* which $\Delta\epsilon_m > V^2/2$,

$$\frac{R_m}{R_s} = \frac{1}{2} \left(\frac{c}{V}\right)^2 \left(\frac{\delta M}{M}\right)^2, \quad (18)$$

where $R_s = 2GM/c^2$ is the Schwarzschild radius and c is the speed of light. Both $\delta M/M$ and V depend on the mass ratio and on the magnitudes and directions of the spins of the merging black holes. To evaluate R_m we use the analytic expressions, calibrated against simulations, given by Tichy & Marronetti (2008) and Miller et al. (2007) respectively. The resulting value of R_m/R_s is shown in Fig. 6, for three different configurations of the black hole spins (a_1 , a_2). For some choices of the parameters, two different magnitudes for the mass loss are associated with the same V , explaining the double valued behaviour of R_m^2 . The figure shows that the larger the kick, the smaller the radius of influence of the mass loss, approaching the innermost stable orbit for the most extreme recoils.

² While δM depends only on the total energy emitted in gravitational waves, V depends also on the degree of asymmetry of the emission. Therefore, two different configurations at merger can release different total energy but carry away the same momentum.

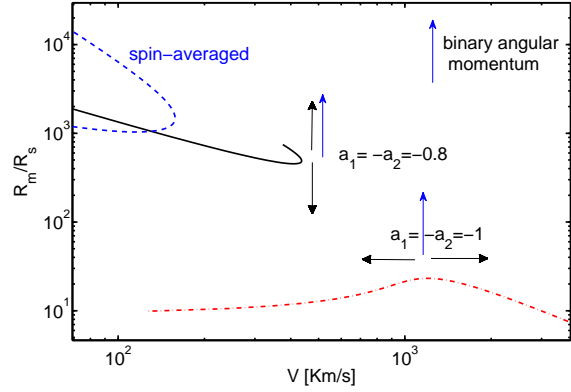


Figure 6. Radius within which $\Delta\epsilon_m$ dominates over $V^2/2$ as a function of the kick velocity V . The dashed line is an average over the spins, assuming isotropic distribution of spin orientation (it amounts to the curve for the kick velocities due only to different mass ratios for the BHs). The solid line assumes equal magnitude spins, aligned with the orbital angular momentum vector but pointing in opposite directions. Finally, the dot-dashed line is for equal magnitude spins, in the direction perpendicular to the orbital angular momentum and anti-aligned.

In our simulations, we verify that for our set-up the dissipation from mass loss is indeed negligible at all times. We will show an example of how the lightcurve from the recoil compares with that of the mass loss for an in-plane kick in Section 4.4.

3 SIMULATIONS

Our analytic predictions are based upon a *particle* rather than a *fluid* model for the disc. Thus, we have run a set of simplified numerical hydrodynamic simulations, in order to check these predictions, and to obtain the explicit form of the energy dissipation rate within the disc as a function of time. We discuss first the special cases of perpendicular ($\theta = 90^\circ$) and in-plane ($\theta = 0^\circ$) kicks. The perpendicular case is exactly axisymmetric, while the in-plane case is also a two-dimensional problem (in r and ϕ) in the limit of an infinitesimally thin disc. Given their symmetry, these cases can be simulated efficiently using Eulerian finite difference methods. The general case of out-of-plane kicks and the $\theta = 0^\circ$ case when the disc has a finite thickness are fully three-dimensional, and correspondingly more difficult. We treat these cases using the Lagrangian Smoothed Particle Hydrodynamics (SPH) method (Gingold & Monaghan 1977; Benz 1990; Monaghan 1992). We compare the two numerical methods by simulating the $\theta = 90^\circ$ case with both codes.

3.1 Initial set-up

We investigate a thin disc, extending from $r = 0.1$ to $r = 10$, in order to encompass the three regions described in Section 2.1. The radial distribution of surface density and sound speed, c_s , are power-laws

$$\Sigma(r) \propto r^{-p} \quad (19)$$

$$c_s(r) \propto r^{-3/4}, \quad (20)$$

with the normalization of the sound speed chosen such that the disc aspect ratio $H/R = 0.05$ at the characteristic radius R_V . The initial conditions of the simulations are isothermal with a fixed (in time)

but radially dependent sound speed. In the finite difference runs the sound speed profile at later times remains fixed (in Eulerian coordinates), whereas in the SPH run the internal energy per unit mass of each *particle* remains constant (i.e. the sound speed is fixed in a Lagrangian sense). In either case the physical assumption is that the energy dissipated as the disc readjusts to its new equilibrium configuration is radiated away rapidly. Since we do not include the effects of the disc self-gravity, the surface density normalization is arbitrary. We can freely scale our results to represent a particular choice of the disc to black hole mass ratio $q = M_d/M$.

The unperturbed — pre-kick — disc velocity field is set to give centrifugal equilibrium in the black hole gravitational field (assumed to be Newtonian). The correction arising from radial pressure gradients within the disc is taken into account, even if it is small for the thin discs that we consider. Working in the frame co-moving with the black hole, the initial (perturbed) velocity field is a superposition of Keplerian anticlockwise rotation with a kick of magnitude V , directed at an angle θ from the disc.

3.2 Numerical implementation

As mentioned above, we performed numerical simulations using two very different schemes. We have compared the corresponding results in order to check that they are numerically reliable. In this section we give an overview of both codes, and in particular note those features that are most important for understanding our conclusions.

We model the effect of an in-plane or perpendicular kick using the ZEUS code (Stone & Norman 1992). ZEUS is a Eulerian finite-difference code. For in-plane kicks we use cylindrical polar co-ordinates (r, ϕ) , assuming symmetry in the z direction. For perpendicular kicks we use spherical polar co-ordinates (r, θ) , assuming symmetry in ϕ . We impose outflow boundary conditions at the inner and outer edges of the grid. Outflow boundary conditions are implemented in ZEUS by setting the gradient of all physical quantities to zero at the boundary. This is exact only for supersonic outflow. Exploratory runs showed that for in-plane kicks enough accretion occurs to bring subsonic gas into contact with the inner boundary. This leads to unphysical reflections. To ameliorate this, we additionally impose a near-vacuum in the innermost active grid zone by sweeping away gas above some small threshold on every time step.

SPH is a Lagrangian code to solve the hydrodynamics equations. Our version of the code self-consistently includes the so-called ∇h terms needed to ensure energy conservation (Monaghan 2007), where h is the smoothing length, which sets the effective resolution length of the simulation. The smoothing length is adjusted adaptively in the code, ensuring higher resolution in high density regions. For a disc with surface density and sound speed profiles as in equations (19) and (20), with $p = 3/2$, the azimuthally averaged smoothing length $\langle h \rangle \propto H$. Therefore, this disc vertical structure is equally resolved at each radius. We have run SPH simulations using different total number of particles N in order to check for convergence. We have found that our results, and in particular the expected luminosity arising from the kick, converge at high resolution, for $N > 4$ million. In the following we present only results corresponding to our highest resolution simulations, which employ either 4 or 8 million particles.

Both codes use artificial viscosity to capture shocks. In our simulations the stress tensor associated with artificial viscosity enters the momentum equation but is neglected in the energy equation (indeed, no energy equation is required in our isothermal runs).

Nonetheless, we can compute the *implied* rate at which viscosity is dissipating kinetic energy in shocks and compressions. Use this to measure the spatial and temporal dependence of the energy dissipation caused by the kick.

In ZEUS, in one spatial dimension (say r) the implied rate of change of the internal energy per unit volume e is,

$$\frac{\partial e}{\partial t} = -Q \left(\frac{\Delta v_r}{\Delta r} \right), \quad (21)$$

where $\Delta v_r = v_{r,i+1} - v_{r,i}$ is the change in velocity across one cell of width Δr and,

$$Q = \begin{cases} C\rho (\Delta v_r)^2 & \text{if } \Delta v < 0 \\ 0 & \text{otherwise.} \end{cases} \quad (22)$$

The dimensionless constant C controls the numerical width of shock fronts. We use $C = 2$. Following the operator-split approach used throughout ZEUS we calculate the full heating rate by adding independent one-dimensional terms in r and ϕ (for in-plane kicks) or r and θ (for perpendicular kicks).

In the SPH code the fundamental quantity is the energy per unit mass u . The implied rate of change of u due to artificial viscosity is

$$\frac{\partial u}{\partial t} = -\frac{Q}{\rho} \nabla \cdot \mathbf{v}, \quad (23)$$

where the divergence of the velocity is calculated over a smoothing length h and the artificial viscosity term Q is

$$Q = \begin{cases} \alpha c_s h \nabla \cdot \mathbf{v} + \beta h^2 (\nabla \cdot \mathbf{v})^2 & \text{if } \nabla \cdot \mathbf{v} < 0 \\ 0 & \text{otherwise.} \end{cases} \quad (24)$$

We use the viscosity switch described in Morris & Monaghan (1997), where the parameter $\beta = 2\alpha$ and α varies from 1 to 0.01 so that dissipation is enhanced when the particle enters the shock region and reduced otherwise.

We note that the quadratic terms for artificial viscosity are essentially equivalent in the two codes, although the SPH implementation is *not* operator split. To calculate the total luminosity that is released (thereafter labelled “implied dE/dt ”), we sum the implied rate of energy dissipation (equation (22) or equation (24)) over volume for ZEUS, and over mass for SPH.

4 NUMERICAL RESULTS

In the following, results are presented in code units in which the unit length is taken to be

$$R_V = GM/V^2 \quad (25)$$

and the unit time is the dynamical time

$$t_V = \left(\frac{GM}{V^3} \right), \quad (26)$$

at R_V , where V is the kick velocity and M the black hole mass. A unit time in code units thus translates to $t = 155$ yr for a black hole mass of $M = 10^6 M_\odot$ and a kick velocity $V = 300$ km s⁻¹. The scaling for the energy dissipation rate is,

$$L = \left(\frac{q}{q_{\text{code}}} \right) \left(\frac{V^5}{G} \right) \times \frac{dE}{dt}, \quad (27)$$

where dE/dt is the implied dissipation rate in code units, $q = M_d/M$ is the actual mass ratio between disc and black hole and $q_{\text{code}} = 6 \times 10^{-4}$ is a fiducial value that we use when plotting the derived energy dissipation rate. For the same kick parameters given

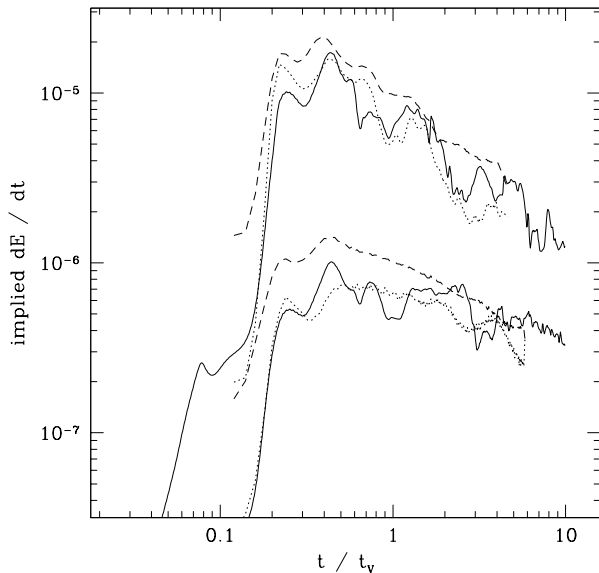


Figure 8. Comparison of the implied energy dissipation rate evaluated from ZEUS (solid curves) and SPH (long dashed curves) simulations for perpendicular kicks. The upper curves show results for steep surface density profiles ($p = 3/2$), the lower curves results for $p = 3/5$. The dotted curves show the portion of the implied SPH dissipation that arises from the quadratic term in the artificial viscosity.

above and $q = q_{\text{code}}$, a typical code luminosity of 10^{-4} then corresponds to a physical luminosity of $3.6 \times 10^{40} \text{ erg s}^{-1}$. Note that the peak luminosity depends upon the ratio of the disc mass to the black hole mass and – very sensitively – on the kick velocity, but that there is no dependence upon the black hole mass.

4.1 Results for perpendicular kicks

To model perpendicular kicks we use ZEUS in its axisymmetric spherical polar mode. For these runs the computational grid extends from $r = 0.025$ to $r = 12$, and $0 < \theta < \pi$. The disc is set up in vertical hydrostatic equilibrium with the mid-plane in the equatorial plane. The disc extends from $r = 0.1$ to $r = 10$. All luminosities are scaled to represent a disc mass ratio $q_{\text{code}} = 6 \times 10^{-4}$. We use 200 mesh points logarithmically spaced in r , and 200 mesh points in θ .

Fig. 7 shows the evolution of the density in the (r, z) plane for a disc with a surface density profile $\Sigma \propto r^{-3/2}$. There is a clear distinction between the behaviour of the gas in the bound and unbound regions, which in this case are radially separated at $r = r_b = r_{\text{ub}} = 1$. The bound gas is distorted by the kick into a bowl-like shape, which oscillates before settling back into the equatorial plane. The unbound gas departs on an essentially ballistic trajectory. A low density streamer of gas that is marginally bound persists out to quite late times.

The energy dissipation rate is plotted as the solid lines in Fig. 8. The luminosity peaks at about $t/t_v = 0.4$ for both of the surface density profiles that we simulated ($p = 3/2$ and $p = 3/5$), before declining slowly out to late times. The oscillations seen after the peak are present in both the SPH and the ZEUS results and also in ZEUS simulations run at different resolutions. Thus they appear to be physical. Since they do not appear for other kick angles they

are probably associated with the dissipation of vertical shear in the 90° case.

4.1.1 Numerical tests

Fig. 8 also shows a comparison between the ZEUS light curve and that derived from the corresponding SPH simulation of the same system. The SPH simulation – which we discuss in more detail in §4.5 – is fully three-dimensional (and hence not optimal for modelling an axisymmetric problem) but is otherwise set up and analysed in a manner that is as close as possible to the ZEUS run. There are two main differences. First, individual SPH particles (whose smoothing length can vary with time) have a fixed internal energy, whereas in the ZEUS runs the sound speed is fixed in Eulerian coordinates. Second, the SPH viscosity used for computing the implied dissipation is similar but not identical to that used in ZEUS. In particular, it includes both a linear and a quadratic term in the divergence of the velocity field (see eq. 24 and eq. 22). Despite these differences we find good agreement between the light curves derived from the SPH (dashed lines) and ZEUS (solid lines) simulations. The agreement is both in the overall normalization and in the rate of decay past the peak. The agreement is not, however, perfect. In order to identify the source of the discrepancy we calculated the implied SPH dissipation due solely to the quadratic term in the artificial viscosity. The resulting light curve is also shown as the dotted line in Fig. 8: it is in significantly better agreement with the results of the ZEUS runs. This leads us to conclude that the different treatment of the artificial viscosity is the main source of differences between the two codes predictions.

We have also tested how sensitive the results are to the magnitude of the artificial viscosity. The potential for unphysical numerical dissipation requires particularly careful consideration for the case of perpendicular kicks, since in this case the initial perturbation is an $m = 0$ warp that gives rise to a wave (Lubow & Pringle 1993; Ferreira & Ogilvie 2008). How such a wave physically dissipates is not obvious. To test the numerical reliability of the derived light curves, we have run additional $\theta = 90^\circ$ simulations that differ by a factor of two in linear resolution (ZEUS, not plotted) or in mass resolution (SPH, shown later in Fig. 13). The higher resolution runs have lower effective numerical viscosity than the lower resolution realizations. For both sets of runs, we find that the shape and magnitude of the light curve *near the peak* is independent of the strength of the numerical viscosity. On the other hand, the very early-time behaviour of the ZEUS light curve is found to be resolution (and thus viscosity) dependent in the sense expected if the dissipation is a numerical phenomenon.³ Our conclusion from these tests is that the very early rise of the luminosity cannot be accurately modeled without the use of a physical model for wave dissipation within the disc. The behaviour of the light curve near the peak, conversely, appears to be robust and well-captured by the code viscosity. We interpret this robustness as being due to the much more violent fluid motions associated with the large distortions seen in Fig. 7.

4.2 Results for in-plane kicks: razor-thin discs

In-plane kicks were also simulated using both ZEUS and SPH. It is important to realize at the outset that, unlike in the case of per-

³ Higher resolution reduces the luminosity by an amount that is roughly consistent with the reduction in artificial viscosity.

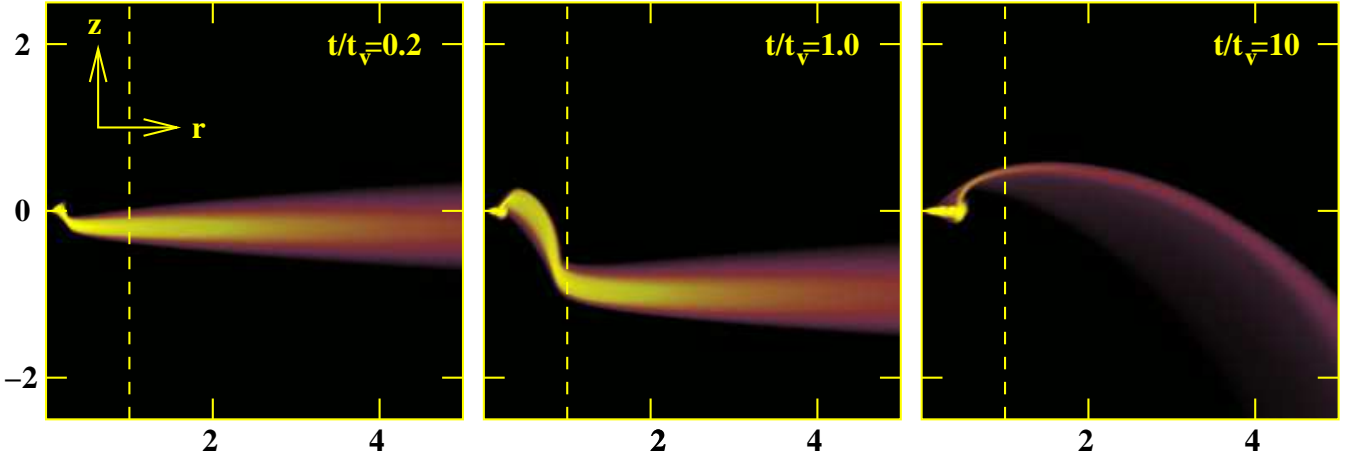


Figure 7. Visualization of the density in the (r, z) plane ($0 < r < 5$, $-2.5 < z < 2.5$) following a kick perpendicular ($\theta = 90^\circ$) to a disc with a surface density profile $\Sigma \propto r^{-3/2}$. By the end of the simulation the unbound material has been lost while the remaining bound disc has largely settled back into the equatorial ($z = 0$) plane. The dashed vertical line in each image marks the cylindrical radius $r = 1$.

pendicular kicks, the ZEUS and SPH simulations of in-plane kicks model *different physical systems*. Our ZEUS runs are strictly two-dimensional in (r, ϕ) , and thus model a razor-thin disc with a vertical thickness that is both negligible and constant with radius. Our SPH runs, on the other hand, model the effect of the same kick on a three-dimensional disc whose scale height is non-zero and increasing with radius. Although the resulting motions are still predominantly confined to the (r, ϕ) plane, the three-dimensional structure of the disc allows gas from large radii to flow inward over the surface of the disc ballistically *without* forming a prompt shock as is inevitable in a strictly two-dimensional system. As we will show, this results in significant changes to the resulting light curve. Here we discuss the ZEUS results, deferring the SPH results to §4.5, where they are presented as part of the investigation of arbitrary kick angles. We emphasize that it is not obvious which model is closer to physical reality. A real disc is of course three-dimensional, as modeled with SPH, but it is also much thinner, at the radii of interest, than the disc simulated numerically and hence arguably closer to the ZEUS razor-thin limit.

For the ZEUS simulations of in-plane kicks the computational grid extends from $r = 0.02$ to $r = 12$, with the initial disc occupying the radial range $0.1 < r < 10$. For this case, $r_b = 0.172$ and $r_{ub} = 5.8$. We use 400 grid points in r , logarithmically spaced to give a radial resolution $r_{i+1}/r_i \approx 1.016$ at all radii, and 300 grid points in ϕ . All luminosities are scaled to represent a disc mass ratio $q_{code} = 6 \times 10^{-4}$.

The evolution of the surface density in the kicked disc is shown in Fig. 9 for the case of a steeply declining surface density profile with $p = 3/2$. We identify three main phases to the evolution, which can be matched to different parts of the bolometric light curve plotted in Fig. 10. In the initial phase, a wave propagates outward through the disc, depositing energy in annuli at successively larger radii. The rate of energy deposition in the symmetric bound region of the disc ($r < r_b = 0.172$), which includes both dissipation of the prompt energy input and accretion energy, peaks at $t/t_v = 0.065$. For the $p = 3/2$ model in which there is a substantial amount of mass at small radii, the overall luminosity peaks shortly afterwards ($t/t_v = 0.08$). The wave then moves on through the outer regions of the disc, during which time the luminosity decays roughly as a power-law with an index $s \approx -0.6$. This phase ends at about the time when the wave reaches the outer

edge of the disc. Afterwards, there is an intermediate period during which the total luminosity declines steeply. Finally, there is a phase in which the luminosity arises from the infall of low angular momentum gas into the inner regions of what remains of the disc. Inspection of animations of the simulation shows that the infalling gas shocks and enters the disc as dense streams. The inner disc at late times is highly non-axisymmetric and time variable. The associated dissipation rate is approximately constant but with large amplitude fluctuations (see also Fig. 11).

The same general behaviour is observed regardless of the choice of initial surface density profile, though there are changes to the slope of the light curve during the first phase and to the amount of low angular momentum material that eventually accretes. Fig. 11 shows the energy dissipation rate in a disc that has the same total mass but a shallower surface density profile ($p = 0.6$). As expected, the amount of energy dissipated in the outer annuli, whose contribution peaks at later times, is increased relative to the $p = 3/2$ disc model. As a result, the total luminosity from the disc rises throughout the first phase, with a power-law index $s \approx 0.15$, until the wave leaves the disc. Since the duration of the energy release is somewhat more extended the peak luminosity is also reduced.

4.3 Surface density evolution

The different behaviour seen for in-plane kicks and perpendicular kicks appears to reflect the increased importance of kick-induced accretion for small kick angles. This is shown in Fig. 12, where we plot the evolution of the surface density of the bound portion of the disc for the in-plane (upper panel) and perpendicular (bottom panel) runs. For the perpendicular kick case we find that after the kick the inner disc settles back to a surface density profile that is very similar to that originally imposed. Note that this settling process takes some time, and it is complete only out to $r \approx 0.5$ by $t/t_v = 10$. A negligible amount of gas ends up interior to the original inner edge of the disc. In contrast, there is substantial accretion in the $\theta = 0^\circ$ run, and this is evident even at early ($t/t_v = 0.1$) times when the light curve is undergoing its initial rise.

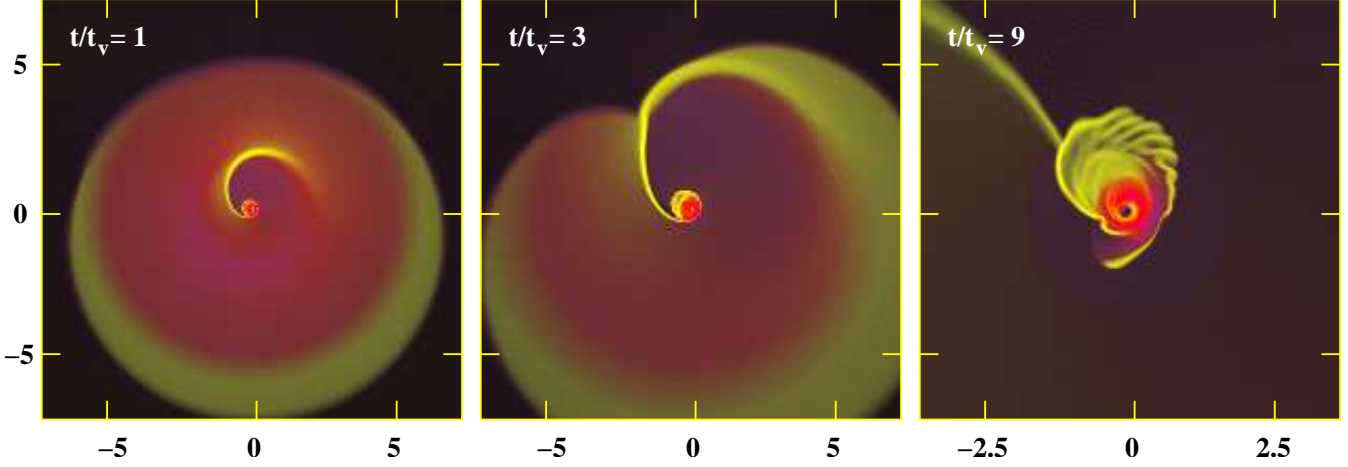


Figure 9. Rendering showing the evolution of the surface density of the disc following an in-plane kick. In this high resolution simulation the disc extends up to $r = r_{\text{ub}}$. During the peak phase of energy dissipation (left-hand panel) energy is dissipated at successively larger disc radii as an outward moving wave propagates through the gas. The outer part of the disc is unbound and escapes ballistically. After the wave reaches the outer edge of the disc (centre panel) the rate of decay of the energy dissipation rate steepens markedly. At late times (right-hand panel, spatial and colour scale adjusted to show structure in the innermost regions) low angular momentum gas continues to accrete on to the bound remnant of the original disc, releasing energy at a low level and forming a highly non-axisymmetric accretion flow.

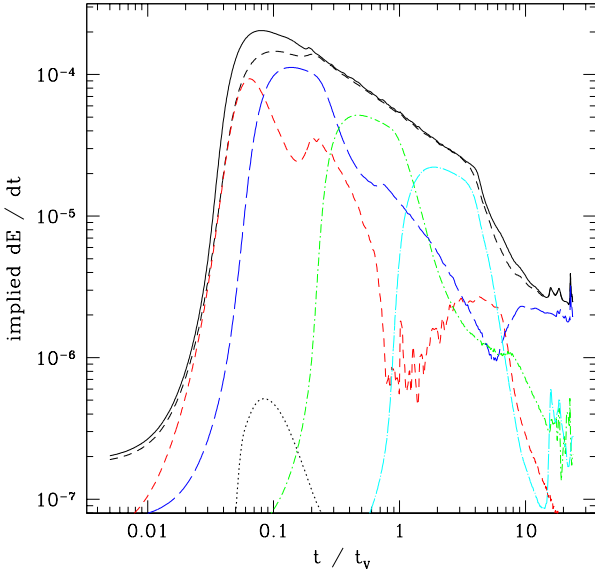


Figure 10. The implied energy dissipation rate as a function of time for an in-plane kick into a razor-thin disc with a surface density profile $\Sigma \propto r^{-3/2}$ and a fixed sound speed profile $c_s \propto r^{-3/4}$. The disc extends up to $r = 10$. Time is measured in units of the dynamical time (t_V) at R_V , while the energy dissipation rate is in code units for a disc mass $M_d/M = 6 \times 10^{-4}$ between $r = 0.1$ and $r = 10$. The solid black curve shows the total energy dissipation rate evaluated across the whole computational domain, while the dashed black line is the dissipation rate for $0.1 \leq r \leq 10$ for comparison with the SPH results. This latter has been divided up into individual contributions from annuli at successively greater radii: $0.1 < r < 0.172 = r_b$ (red short-dashed line), $0.172 < r < 0.55$ (blue long-dashed line), $0.55 < r < 1.79$ (green dot-dashed line) and $1.79 < r < 5.8 = r_{\text{ub}}$ (cyan dot-long-dashed line). The dotted black curve (at the bottom) shows the result for a disc with no kick but an instantaneous black hole mass loss of $0.03M$.

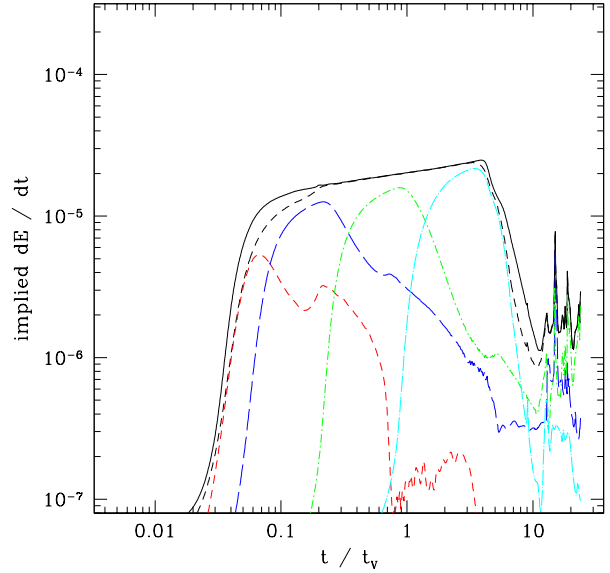


Figure 11. The implied energy dissipation rate as a function of time for a disc with a flatter surface density profile $\Sigma \propto r^{-3/5}$. The total energy dissipation rate (shown as the solid black curve) peaks at a smaller value than for $\Sigma \propto r^{-3/2}$. Light curves for individual annuli are plotted as in Fig. 10, except that no mass-loss light curve is shown here.

4.4 Mass-loss simulation

Fig. 10 also shows how the energy dissipation rate in the disc due to the kick compares to that which would arise as a result of the black hole mass loss experienced upon merger (the dotted line at the bottom of the figure). For simplicity we set up a disc model identical to that used for the kick simulation, but set $V = 0$ and imposed an instantaneous mass loss of 3%. The simulation was run until $t/t_V = 2$. Given our parameters, the energy dissipation rate in

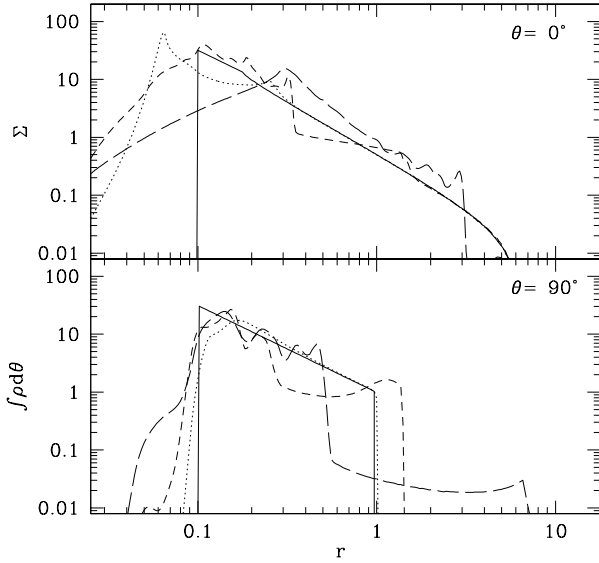


Figure 12. Evolution of the disc surface density with time from ZEUS simulations of kicks at $\theta = 0^\circ$ (upper panel) and $\theta = 90^\circ$ (lower panel) to the disc plane. For clarity only gas that remains bound to the black hole is included in the calculation of the surface density. Both discs had initial surface density profiles $\Sigma \propto r^{-3/2}$. (solid lines, plotted here in arbitrary units). Additional curves show the profile at $t/t_V = 0.1$ (dotted lines), $t/t_V = 1$ (short-dashed lines) and at the end of the simulations (long-dashed lines plotted at $t/t_V = 20$ for the in-plane run and $t/t_V = 10$ for the perpendicular kick).

the disc induced by the mass loss peaks early ($t/t_V = 0.085$) at a luminosity that is more than two orders of magnitude below that generated by the kick. We can therefore consistently ignore black hole mass loss in our simulations. Of course this does not mean that mass loss is always *physically* negligible, since (to quote a trivial example) mass loss must occur in mergers whose symmetry is such that no recoil is produced. The analytic discussion in Section 2.5 provides an estimate of when mass loss might be competitive as a source of disc energy dissipation.

4.5 Results for out-of-plane kicks

In this Section, we discuss the results of SPH simulations of discs subject to kicks at arbitrary angles. Our simulations are for kick angles $\theta = 0^\circ$ (with a finite thickness disc), $\theta = 15^\circ$, $\theta = 30^\circ$, $\theta = 60^\circ$ and $\theta = 90^\circ$. As previously, we adopt a nominal disc to black hole mass ratio $q = 6 \times 10^{-4}$. As an initial numerical check we show in Fig. 13 the light curves for $\theta = 30^\circ$ and $\theta = 90^\circ$ at two different resolutions: 4 million particles (dashed line) and 8 million particles (solid line). Excellent agreement is obtained, providing evidence that our simulations have converged. This result, together with the results of the code comparison at $\theta = 90^\circ$, makes us confident that any uncertainties in the numerical computation of the light curves from the SPH simulations are small. For practical purposes, they are certainly much smaller than physical uncertainties arising, for example, from poor knowledge of the actual initial surface density profile at the relevant radii.

Visualisations of the evolution of the column density from the $\theta = 30^\circ$ run are shown in Fig. 14 (edge-on view) and in Fig. 15

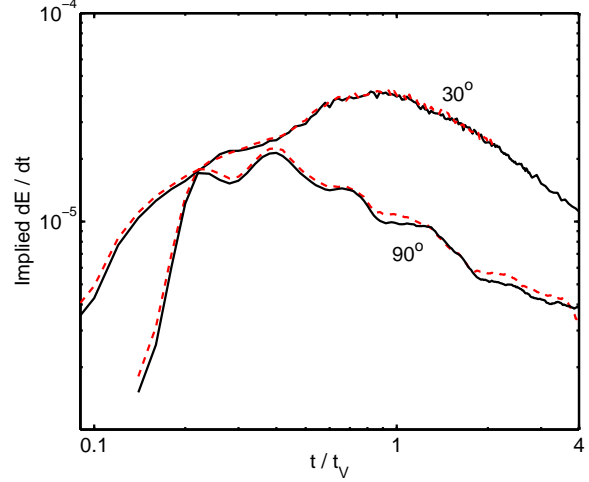


Figure 13. Light curve obtained for $\theta = 30^\circ$ and $\theta = 90^\circ$, from SPH simulations at two different resolutions: 4 million particle run (red dashed lines) and 8 million particle run (solid black lines).

(face-on view). For this kick angle the two characteristic radii are approximately equal to $r_b \approx 0.2$ and $r_{ub} \approx 4.8$, respectively. Although the geometry is now more complex the overall behaviour resembles that seen in the special cases discussed earlier. As the black hole is ejected from the centre of the disc it carries with it the innermost part of the disc, while the outer part lags behind and is dispersed. The bound mass in the simulation agrees with that predicted analytically and is constant with time. The edge-on images show that there is a brief initial phase during which the disc is warped, but as was found for $\theta = 90^\circ$, the gas quickly readjusts to orbit within a single plane. In this case, however, the plane is tilted with respect to that of the original disc (see discussion in §2.2). The face-on images show that the final extent of the remnant disc is comparable with r_b . As we will see in the following section, most of the dissipation occurs in this region ($r \lesssim r_b$).

The implied rate of energy dissipation as a function of time is plotted in Fig. 16 with a black solid line. The contribution to the light curve from gas at different distances from the black hole is shown in the same figure. We have divided the disc into three broad annuli: $0.1 < r < r_b$, $r_b < r < r_{ub}$ and $r > r_{ub}$. Within each annulus, we computed the energy dissipation rate by summing over all particles that are *instantaneously* within that region. As was the case for the in-plane kick, we see an initial rise in the luminosity as the compression wave propagates outwards and energy is dissipated at successively larger radii. The peak in the total curve at $t \approx 0.9$ is primarily due to dissipation in the inner region ($r < r_b$), although material in the intermediate zone $r_b < r < r_{ub}$ – whose contribution dominates the light curve during its declining phase – is responsible for a substantial amount of energy when integrated over time. Within this ring ($r_b < r < r_{ub}$) most of the dissipation occurs close to r_b . The contribution to the light curve from gas at $r > r_{ub}$ is negligible and consistent with zero, as we assumed in the analytic calculation⁴.

We also note that both the total light curve and the light curves of the two individual rings within r_{ub} show some evidence for a two-component structure. The presence of two components is more

⁴ We verified in particular that particles *originally* at $r > r_{ub}$ are lost without encountering shocks or compressions that result in significant heating.

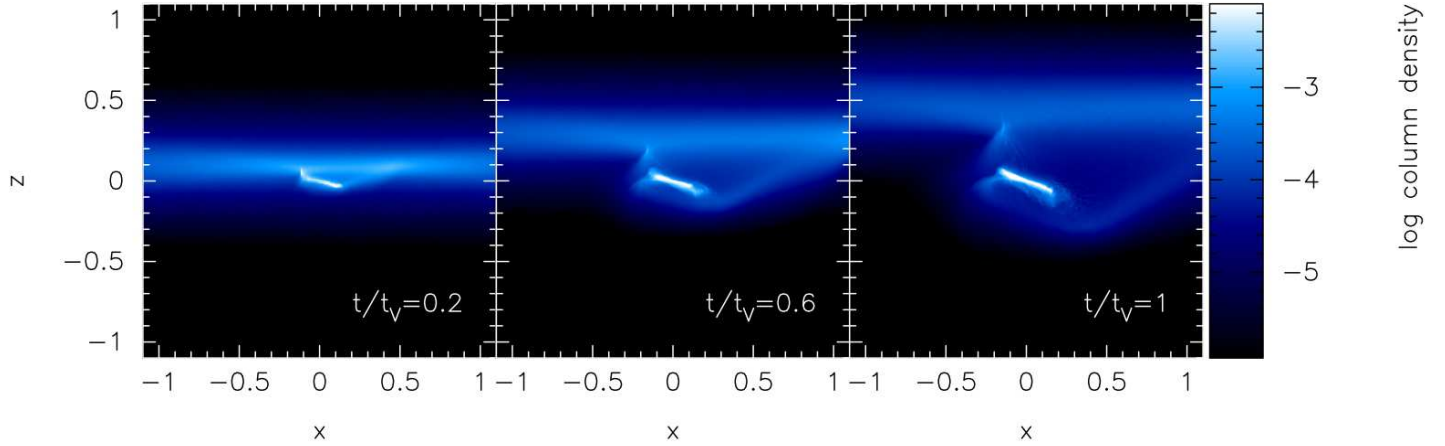


Figure 14. Visualization of the column density (in code units) at different times, from a simulation with a kick at $\theta = 30^\circ$. Part of the disc remains bound to the black hole, and this material rapidly settles into a relatively stable tilted configuration. Unbound gas can be seen leaving the system in the upper portion of the panels.

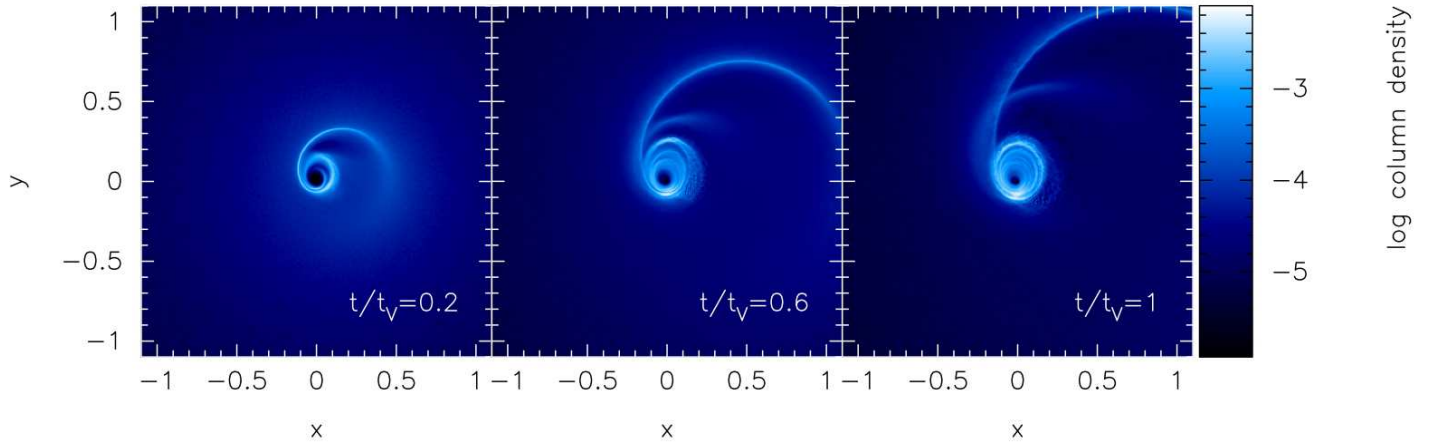


Figure 15. Visualization of the column density (in code units) through the disc at different times, from a simulation with a kick at $\theta = 30^\circ$. In this face-on view, structure analogous to that seen in the $\theta = 0^\circ$ simulations is clearly visible.

clearly seen in the $\theta = 15^\circ$ light curve, shown as Fig. 17. For this figure we have computed the dissipation not only as a function of the *current* radius of particles within the disc (upper panel), but also by binning the particles depending upon their *initial* location (lower panel). This allows us to (at least partially) separate the contributions from the prompt deposition of kick energy and that arising due to accretion. We find that most of the dissipation occurs within r_b (upper panel). At early times this dissipation is partially associated with gas that originated in this region (lower panel), and we thus infer that the initial rise (up to and through the first shallow peak) in luminosity is due to both prompt dissipation of kick energy and accretion that involves small changes in orbital radius. The second more prominent peak, on the other hand, occurs as energy is dissipated within r_b (upper panel) in gas that was mostly originally in the region between r_b and r_{ub} (lower panel). We identify this contribution as being almost entirely due to accretion of low angular momentum matter that falls from larger radii and deposits energy

at smaller radii. The deposition occurs via mild shocks and this may cause matter to lose additional angular momentum, sink further toward the centre and therefore release additional potential energy.

In order to quantify whether accretion occurs beyond the level expected from angular momentum conservation, we have made use of the Lagrangian nature of SPH: we plot the final ($t/t_V = 8.5$) radial position of bound particles as a function their initial position on a particle-by-particle basis (Fig. 18). The data are from the $\theta = 30^\circ$ simulation. In Fig. 18, the red line shows the locus where particles should lie if they conserved their angular momentum (equation 7). We find that to a *first approximation* angular momentum conservation is a good assumption. However, there is clearly a trend for the bound gas – especially from $r_b < r < r_{ub}$ – to fall deeper into the potential well, and form a remnant disc that is smaller than would be predicted under our assumption. This is the result of angular

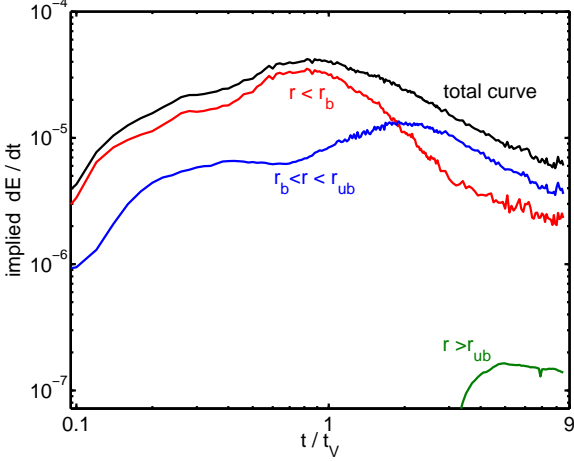


Figure 16. Light curve derived from an SPH simulation of the $\theta = 30^\circ$ case. dE/dt is in code units. Here we also show the individual contributions arising from energy dissipated in three different radial regions as marked. Clearly most of the dissipation occurs within R_{ub} .

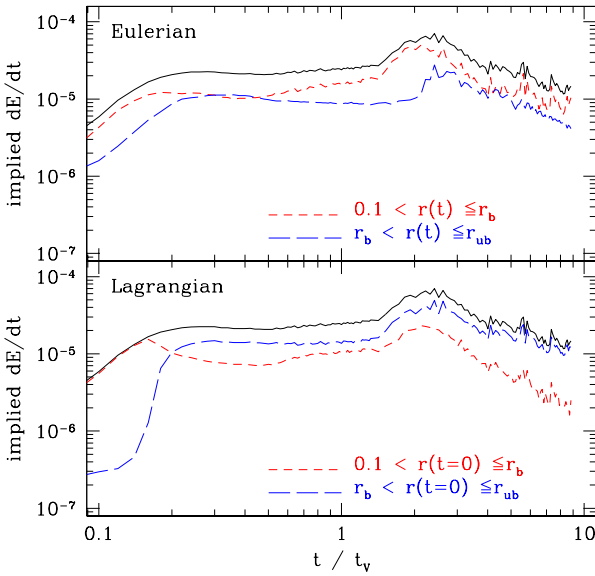


Figure 17. Light curve for $\theta = 15^\circ$ in code units. This particular simulation used 4 million particles. *Upper panel:* The total dissipation rate (black solid line) is the sum of the energy dissipated within r_b (red short-dashed line) and between r_b and r_{ub} (blue long-dashed line). These contributions are calculated summing over particles present at that time in the region. *Lower panel:* the same as above, but here we show the individual contributions of those particles initially (at $t = 0$) within r_b (red short-dashed line) and between r_b and r_{ub} (blue long-dashed line).

momentum mixing, where particles with larger initial angular momentum transfer part of it to particles with an initially lower one.

The final formation of a relatively compact disc can also be seen in Fig. 19, where we plot the evolution of the surface density for this run. Most of the bound particles in the final disc end up within r_b , with a steep tail at larger radii that drops to almost zero by about $3r_b$. This behaviour does not match that predicted from

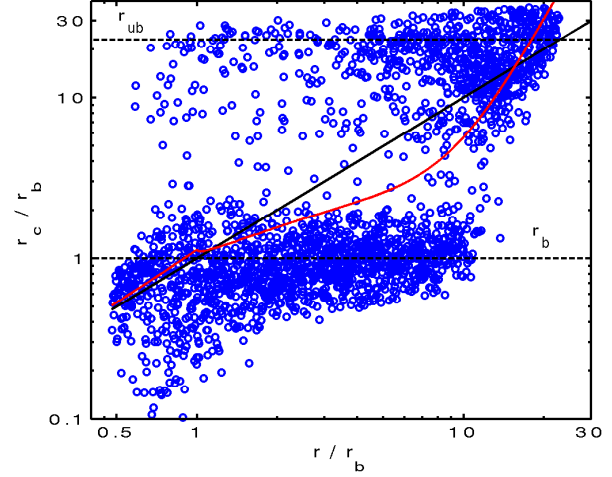


Figure 18. Final (at $t/t_v = 8.5$) radial position of a bound ($\epsilon < 0$) SPH particle in units of r_b as a function of its initial radial position in the same units, for the $\theta = 30^\circ$ case (blue symbols). For clarity, only 10^{-3} of the total bound particles are plotted. For comparison, we plot as the red solid line our analytic expectation (equation 7). The black solid line marks where $r = r_c$.

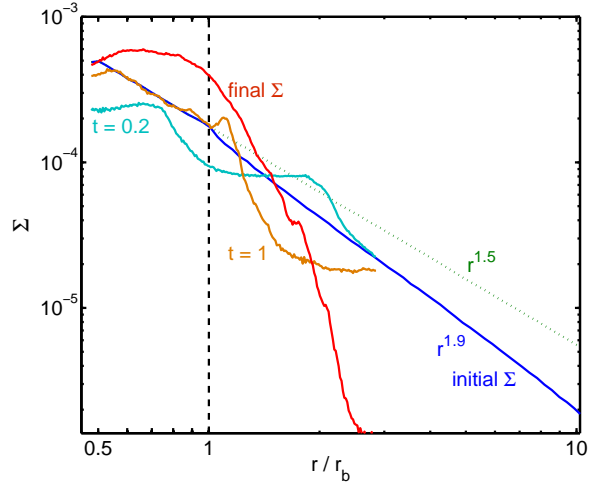


Figure 19. Surface density (code units) as a function of radius. At the beginning of the simulation all particles are distributed with a $r^{-3/2}$ profile, while the bound particles follows a steeper profile of $\Sigma \propto r^{-1.9}$. At the end of the simulation ($t/t_v = 8.5$) the bound particles are mostly within R_b and their surface density distribution falls-off rapidly for larger radii.

the model assuming circularization at constant angular momentum. Rather, there is an indication of angular momentum transfer and additional accretion of matter (see also Fig. 18). Since exact conservation of particle angular momentum was assumed in our analytic model, these results imply that it cannot provide a precise quantitative estimate of the total energy release, but rather (for this kick angle) a lower limit. Longer duration simulations will be needed to determine how much energy in excess of our simple model is indeed dissipated.

The dependence of the shape and amplitude of the light curve on the direction of the black hole recoil is illustrated in Fig. 20. The peak luminosity and the total dissipated energy increase for kicks that are more closely directed toward the disc plane. This trend is

evident for angles of 30° and smaller (the $\theta = 90^\circ$ and $\theta = 60^\circ$ runs are quite similar). The shape of the light curve is a complex function of the kick angle. We interpret the behaviour seen in the simulations as being a consequence of the existence of two components to the light curve, whose separation in time is a function of kick angle. One contribution is associated with gas in the inner disc (within and close to r_b). As the kick angle decreases r_b also shrinks, and the energy dissipated within this region of the disc is released on a shorter time scale. A second contribution, due to accretion, occurs on a time scale that is related to r_{ub} , which *increases* for kicks that are directed closer to the disc plane. The superposition of the two components results in a light curve that is clearly double-peaked only for a narrow range of kick angles, but whose evolution with kick angle qualitatively matches that seen in the simulations.

We also note that the result for the $\theta = 0^\circ$ simulation presented here, for a finite thickness disc, differs significantly from that obtained with ZEUS for a razor-thin disc §4.2 (compare Fig. 20 with Fig. 10). In particular, for the finite thickness disc we do not observe the very rapid rise to peak luminosity seen in the ZEUS simulation. Instead, the $\theta = 0^\circ$ light curve continues the trend toward longer time scale energy release that is seen in the $\theta = 30^\circ$ and $\theta = 15^\circ$ simulations. Analysis of the SPH simulation suggests that the reason for the difference between the two results lies in the presence of three-dimensional flows of gas across the surface of the kicked disc. They cannot occur in a strictly two-dimensional calculation. In the SPH runs the kick causes some of the gas in the outer disc (at relatively large height above the mid-plane) to flow inward over the surface of the disc, before releasing energy at smaller radii and later times. Inspection of the vertical profile of energy dissipation in the SPH run shows a substantial release of energy in the surface layers of the disc.

Finally, we compare in Fig. 21 the cumulative energy release as a function of θ with the analytic estimate discussed in Section 2.5. The figure shows (as the red stars) the total energy release derived by integrating the high and moderate θ light curves shown in Fig. 20 through to the end of the simulations. It is clear that energy dissipation is still ongoing at the (arbitrary) epoch at which the simulations stop, so our estimates of the total release are lower limits. Nonetheless, the simulations clearly show a trend toward increasing energy release for smaller kick angles that – for kick angles between 90° and 15° – agrees surprisingly well with that predicted analytically. For the 0° run (whose integrated energy release is not plotted because the simulation was of shorter duration) the light curve (Fig. 20) shows a further increase in total energy as compared to the 15° run, though we do not find evidence for the very large (in fact divergent) increase predicted analytically. We attribute this difference as being due to the fact that the analytic divergence arises because a small amount of mass in the disc is predicted to circularize at zero radius. Any hydrodynamic mixing suffices to give the initially zero angular momentum gas a small amount of angular momentum, eliminating the divergent behaviour. This results in a smaller total energy release. We caution, however, that the maximum value of the total energy release at small kick angles may well depend upon the physical thickness of the disc, which is larger in the simulations than in real systems. For very thin discs the analytic trend toward increasing energy release might extend to smaller kick angles than those obtained here.

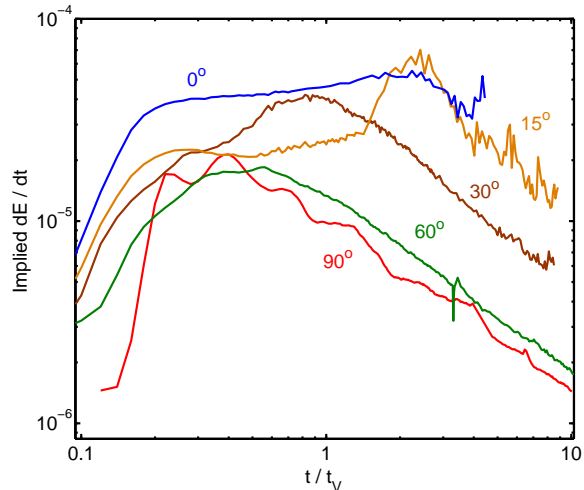


Figure 20. Total (from the whole disc) rate of energy dissipated as a function of time for different recoil directions. The figure shows results from SPH simulations at $\theta = 90^\circ$, $\theta = 60^\circ$, $\theta = 30^\circ$, $\theta = 15^\circ$, together with the in plane case ($\theta = 0^\circ$). All curves have the same disc model with a surface density profile $\Sigma \propto r^{-3/2}$ and a total mass (relative to the black hole) of $q = 6 \times 10^{-4}$ between $r = 0.1$ and $r = 10$.

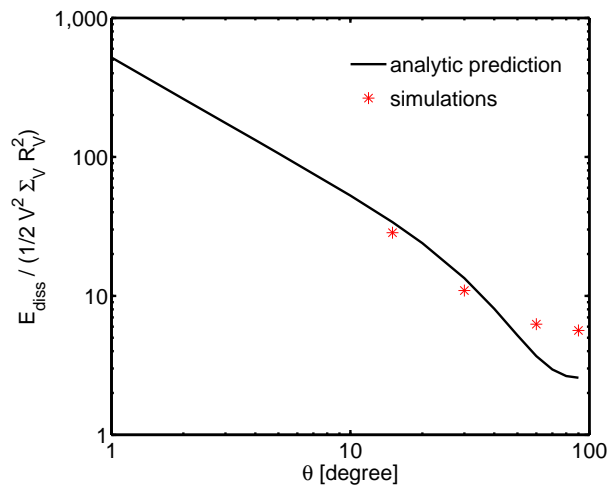


Figure 21. Comparison of the analytic prediction for the total energy release (solid curve) with the simulation results (stars), as a function of kick angle.

5 DISCUSSION

Our numerical results can be scaled to represent a wide range of different systems. In doing so, three parameters enter the problem: (1) the black hole mass, which affects the characteristic time scale t_v over which energy is deposited into the disc, (2) the kick velocity, which affects both the time scale and the normalization of the luminosity, and (3) the disc mass, which alters the luminosity. The effect of kicks on surrounding discs might in principle be observable in two distinct regimes. For *low-mass black holes* with $M \sim 10^6 M_\odot$ the time scales for the initial rise in the light curve in the source frame range from ~ 10 yr for $V = 300 \text{ km s}^{-1}$ down to as little as ~ 1 yr for $V > 10^3 \text{ km s}^{-1}$. It may therefore be possible to detect a time-variable electromagnetic counterpart from the kicked disc following a merger that has been approximately localized by

gravitational-wave (or other) observations (Lippai et al. 2008). For *high-mass black holes* ($M \sim 10^8 M_\odot$) the long time scales for variability and the rarity of mergers in this mass range combine to make such triggered searches unfeasible. It has been suggested, however, that the spectrum of a kicked disc might be sufficiently distinct from that of other sources as to allow identification in wide-area surveys (Schnittman & Krolik 2008).

In addition to the black hole mass and kick velocity, the disc mass is an important parameter, since the luminosity is proportional to the surface density at the characteristic radius R_V . It is important to note that this is a large radius: for $M = 10^6 M_\odot$ and $V = 300 \text{ km s}^{-1}$, we have $R_V = 0.05 \text{ pc}$ ($10^6 GM/c^2$), while for $M = 10^8 M_\odot$ and $V = 10^3 \text{ km s}^{-1}$ we have $R_V = 0.43 \text{ pc}$ ($\approx 10^5 GM/c^2$). At these radii an argument can be made that the maximum surface density of a geometrically thin accretion disc is limited by the onset of fragmentation due to the disc’s self-gravity (Gammie 2001; Goodman 2003; Rice, Lodato & Armitage 2005; Rafikov 2005; for a review see Lodato 2007). A simple estimate can be derived by making use of the steady-state models calculated by Levin (2007). In these models the maximum value of Σ is a function only of Ω , and varies from $\Sigma_{\text{max}} \sim 2 \times 10^3 \text{ g cm}^{-2}$ at a radius where the orbital period $P = 10^2 \text{ yr}$ down to $\Sigma_{\text{max}} \sim 40 \text{ g cm}^{-2}$ or less at $P = 10^3 \text{ yr}$. Writing the maximum disc mass as $M_{\text{max}} \sim \pi R_V^2 \Sigma(R_V)$, where $\Sigma(R_V)$ is the maximum value of the surface density that would be stable against fragmentation at R_V , we find that for a range of kick velocities between 300 km s^{-1} and 10^3 km s^{-1} the disc around a $10^6 M_\odot$ black hole would be unlikely to exceed $q \sim 10^{-3}$ of the black hole mass. In scaling our results to $M = 10^6 M_\odot$, we therefore use the value $q = 6 \times 10^{-4}$ discussed earlier. For a $10^8 M_\odot$ black hole a somewhat more massive disc could be stable, and for this case we scale to $q = 6 \times 10^{-3}$.

Given the important role that the assumed disc mass plays in determining the observability of emission from kicked discs, it is worth stressing that these estimates are crude. There are few observational constraints on discs at sub-pc scales in galactic nuclei. Theoretical work only strictly excludes the existence of *very* massive discs that are heated by viscous processes and cool radiatively. Therefore, it would not surprise us if our “limits” could be exceeded.

Fig. 22 shows examples of the scaled light curves for three sets of parameters: (1) a baseline case with $M = 10^6 M_\odot$, $V = 300 \text{ km s}^{-1}$ and $q = 6 \times 10^{-4}$; (2) a more optimistic (as far as observability goes) case with $M = 10^6 M_\odot$, $V = 10^3 \text{ km s}^{-1}$ and $q = 6 \times 10^{-4}$; and (3) a high mass case with $M = 10^8 M_\odot$, $V = 10^3 \text{ km s}^{-1}$ and $q = 6 \times 10^{-3}$. These parameters are similar to those considered by Schnittman & Krolik (2008) except for the fact that, for the reasons outlined above, we use a substantially smaller disc mass. For each parameter set we plot the total luminosity from the $\theta = 15^\circ$ and $\theta = 90^\circ$ simulations, which roughly bracket the range of likely behaviour seen in our simulations.

The maximum luminosity obtained from the $M = 10^6 M_\odot$ models is $L \simeq 10^{43} \text{ erg s}^{-1}$, which corresponds to about 10% of the Eddington luminosity $L_{\text{Edd}} = 1.3 \times 10^{44} \text{ erg s}^{-1}$ for this mass of black hole. Reaching this luminosity, however, requires a combination of circumstances that may be uncommon: a high velocity kick ($V = 10^3 \text{ km s}^{-1}$), directed almost into the plane of a disc, with a steep surface density profile. The peak luminosity for most of the other models plotted in Fig. 20 is smaller: around $2 \times 10^{42} \text{ erg s}^{-1}$ ($1.5\% L_{\text{Edd}}$) for $V = 10^3 \text{ km s}^{-1}$ and $\theta = 90^\circ$, and approximately $10^{40} \text{ erg s}^{-1}$ ($10^{-4} L_{\text{Edd}}$) for the models with $V = 300 \text{ km s}^{-1}$. These values encompass the range of luminosities ($6.3 \times 10^{-4} L_{\text{Edd}}$ to $1.6 \times 10^{-2} L_{\text{Edd}}$) estimated by Lippai et al. (2008).

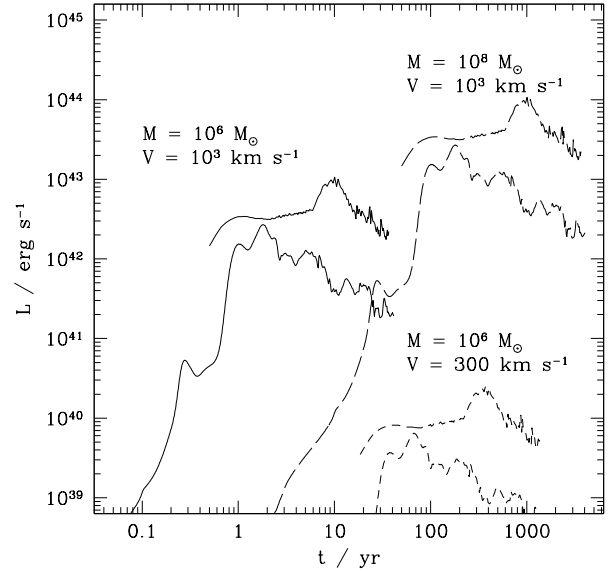


Figure 22. The predicted bolometric light curve of the kicked disc after scaling the numerical results to represent three different classes of systems. The solid curves show the light curves for $\theta = 15^\circ$ (upper curve) and $\theta = 90^\circ$ (lower curve) runs, following scaling to $M = 10^6 M_\odot$, $V = 10^3 \text{ km s}^{-1}$, and a disc mass ratio $q = 6 \times 10^{-4}$. Both runs are for a surface density profile with $p = 3/2$. The short dashed curves are for identical parameters except for a lower kick velocity of $V = 300 \text{ km s}^{-1}$. The long dashed curves are for a system with $M = 10^8 M_\odot$, $V = 10^3 \text{ km s}^{-1}$, and a disc mass ratio $q = 6 \times 10^{-3}$.

Fig. 23 shows the predicted bolometric flux from the disc as a function of source redshift z . We assume a luminosity distances appropriate for a standard cosmology. As expected from the fact that even the most luminous sources are sub-Eddington, none of our sources are predicted to be very bright. Electromagnetic counterparts might be detectable if V lies toward the upper end of the considered range, especially if the merger is nearby. Low velocity kicks ($V = 300 \text{ km s}^{-1}$), on the other hand, yield very low luminosities that would not be detectable at plausible cosmological distances.

Fig. 22 also shows the predicted light curve for a disc around a $10^8 M_\odot$ black hole following a kick of 10^3 km s^{-1} . These parameters have been chosen to match those adopted by Schnittman & Krolik (2008), although our curves are calculated for a steeper surface density profile than the $\Sigma \propto r^{-3/5}$ that they used. Nonetheless we find that (for the $\theta = 15^\circ$ run) the time of the predicted peak ($t \sim 10^3 \text{ yr}$ in the source frame) is similar to that derived by Schnittman & Krolik (2008). The amplitude, however, is more than an order of magnitude lower (about $10^{44} \text{ erg s}^{-1}$ as opposed to a few $10^{45} \text{ erg s}^{-1}$). This difference arises because we have limited the disc mass to the maximum that is allowable before self-gravity would result in fragmentation. Unless there is some way to circumvent this limit, we conclude that the prospects for detecting the emission from kicked discs in surveys are poor.

In addition to the energetic considerations discussed here, the actual observability of emission from kicked discs will also depend upon the spectral band in which the radiation is emitted. We expect emission in the soft X-ray, if the disc is optically thin at the radii of interest, or if the bulk of the energy is ultimately deposited in

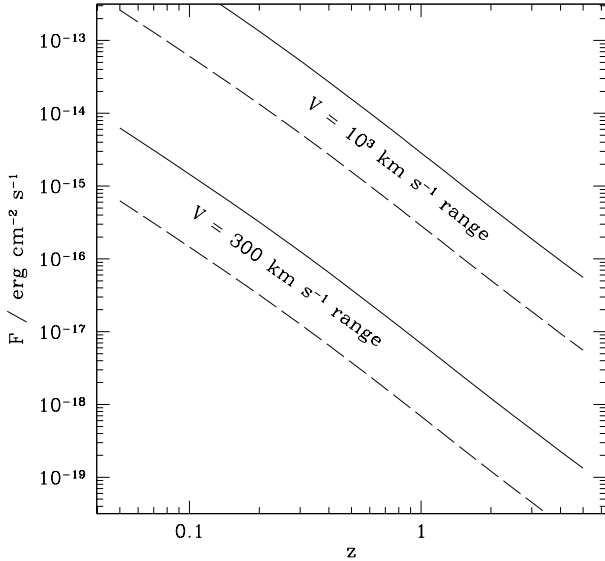


Figure 23. The predicted bolometric flux from the disc as a function of the redshift z of the source is plotted for two kick velocities, $V = 300 \text{ km s}^{-1}$ and $V = 10^3 \text{ km s}^{-1}$. For each velocity we show two curves that approximately encompass the range of peak luminosities implied by our simulations. The lower dashed curves show results for typical kick orientations (corresponding to luminosities in code units of 10^{-5}), while the upper solid curves show results for more optimistic geometries in which the kick is directed close to the disc plane (10^{-4} in code units).

the upper layers of the disc atmosphere. The emission would be at a temperature of $T_X \sim 1 \text{ keV}$, that corresponds to the post-shock value behind a shock of a few hundred km s^{-1} (Lippai et al. 2008; Shields & Bonning 2008). Energy deposition at the midplane of an optically thick disc, conversely, would result in thermal emission in the infrared (Schnittman & Krolik 2008). The results of Levin (2007) imply that self-gravitating discs ought to be optically thick out to radii where the orbital period is $P \approx 600 \text{ yr}$. Hence the high-velocity kicks that are most observable would deposit their energy at radii where the disc was optically thick. We caution, however, that this does not necessarily imply that all of the energy is thermalized into the infrared. Waves within discs can – under certain circumstances – deposit energy preferentially in the low density atmosphere rather than at the disc midplane (Bate et al. 2002). More detailed simulations, that include a realistic treatment of the disc’s vertical structure, will be needed to determine where energy is deposited, and what the resulting spectral signatures are.

6 CONCLUSIONS

In this paper we have investigated the effect of a post-merger kick on the dynamics of a geometrically thin accretion disc, surrounding the newly merged black hole. The existence and strength of kicks following black hole mergers are now secure predictions of General Relativity. Whether small-scale gas discs typically attend mergers remains, however, uncertain. If gas discs are commonly present the perturbation to the gas caused by the kick will generate an electromagnetic counterpart to the merger, which may be detectable if its amplitude and time scale are observable at cosmological distances.

The main conclusions of our study are:

1. The dimensional assumption that the magnitude of energy release is $(1/2)V^2\Sigma_V R_V^2$ is an underestimate. The energy available for dissipation varies strongly with the angle between the kick and the disc plane, and for kicks close to the plane our analytic estimate exceeds $(1/2)V^2\Sigma_V R_V^2$ by up to three orders of magnitude. A large increase in the energy release for kicks close to the plane is confirmed numerically.

2. For most orientations of the kick, accretion energy (i.e. energy liberated when gas in the disc loses angular momentum and falls inward) dominates over the direct energy input to the gas in the frame of the kicked black hole. Accretion energy is particularly important for kicks that are directed toward the disc plane. The importance of accretion can be demonstrated analytically, and is confirmed by numerical simulations.

3. We have run SPH and (for the special cases that are two-dimensional) finite difference numerical simulations to investigate the evolution of the disc and the rate of energy dissipation, following a kick at an arbitrary angle to the disc plane. The simulations yield explicit predictions for the form of the light curves as a function of both kick angle and surface density structure within the disc.

4. The observability of emission from kicked discs depends upon the kick velocity, the orientation of the kick relative to the disc plane, and the mass of the disc at the radii where the energy is deposited. We have argued that the mass of the disc is limited by the requirement that the disc remains stable to fragmentation due to self-gravity. If this is true, the decreased disc mass (as compared to that assumed in prior works) outweighs the effect of the increased energy release per unit mass. As a result, the predicted luminosity around massive black holes is substantially smaller than previously thought. It is unlikely that such sources can be identified via wide-area sky surveys.

5. The most feasible observational probe of the phenomena discussed here is via identification of variable disc emission following black hole mergers detected by other means (e.g. via detection of gravitational waves). Disc emission may be detectable provided that the kick velocity is large, especially in the case where the kick is directed close to the disc plane. To quantify, a kick velocity of 10^3 km s^{-1} offers promising possibilities, but 300 km s^{-1} appears to be very difficult or impossible to detect.

Physically, the magnitude and orientation of the kick is determined by the magnitude and direction of the spin of the black holes immediately prior to their merger. Our results emphasize that the observability of this class of electromagnetic counterparts depends sensitively on the distribution of the pre-merger spins. Studies, such as that by Bogdanović et al. (2007) and that by King, Pringle & Hofmann (2008), that attempt to predict the evolution of black hole spin during the earlier phases of merger are thus particularly important for determining whether counterparts will be detectable. Determining the spectral signature of the kicked disc is also important, and this will require simulations of the disc evolution that include more complete treatments of the disc physics.

ACKNOWLEDGMENTS

The simulations reported in this paper made use of computational facilities at the University of Leicester. Our visualizations made use of the SPLASH software package (Price 2007). P.J.A. acknowledges support from the NSF (AST-0807471), from NASA’s Origins

of Solar Systems program (NNX09AB90G), and from NASA's Astrophysics Theory program (NNX07AH08G).

REFERENCES

- Armitage P. J., Natarajan P., 2002, *ApJ*, 567, L9
- Baker J. G., Boggs W. D., Centrella J., Kelly B. J., McWilliams S. T., Miller M. C., van Meter J. R., 2007, *ApJ*, 668, 1140
- Bate M. R., Ogilvie G. I., Lubow S. H., Pringle J. E., 2002, *MNRAS*, 332, 575
- Benz W., 1990, in Buchler J., ed., *The Numerical Modeling of Nonlinear Stellar Pulsations* Kluwer, Dordrecht
- Bogdanović T., Reynolds C. S., Miller M. C., 2007, *ApJ*, 661, L147
- Callegari S., Mayer L., Kazantzidis S., Colpi M., Governato F., Quinn T., Wadsley J., 2009, *ApJ*, 696, L89
- Chang, P., Strubbe, L. E., Menou, K. & Quataert, E., 2009, *MNRAS*, submitted (arXiv:0906.0825v1)
- Cuadra J., Armitage P. J., Alexander R. D., Begelman M. C. 2009, *MNRAS*, 393, 1423
- Dotti M., Colpi M., Haardt F., Mayer L., 2007, *MNRAS*, 379, 956
- Escala A., Larson R. B., Coppi P. S., Mardones D., 2005, *ApJ*, 630, 152
- Ferreira B. T., Ogilvie G. I., 2008, *MNRAS*, 386, 2297
- Gammie C. F., 2001, *ApJ*, 553, 174
- Gingold R. A., Monaghan J. J., 1977, *MNRAS*, 181, 375
- Goodman J., 2003, *MNRAS*, 339, 937
- Ivanov P. B., Papaloizou J. C. B., Polnarev A. G., 1999, *MNRAS*, 307, 79
- King A. R., Pringle J. E., Hofmann J. A., 2008, *MNRAS*, 385, 1621
- Levin Y., 2007, *MNRAS*, 374, 515
- Lippai Z., Frei Z., Haiman Z., 2008, *ApJ*, 676, L5
- Lodato G., 2007, *Rivista del Nuovo Cimento*, 30, 293
- Lodato G., Nayakshin S., King A. R., Pringle J. E., 2009, *MNRAS*, in press. ArXiv e-prints, 0906.0737
- Lubow S. H., Pringle, J. E., 1993, *ApJ*, 409, 360
- Megevand M., Anderson M., Frank J., Hirschmann E. W., Lehner L., Liebling S. L., Motl P. M., Neilsen D., 2009, ArXiv e-prints, 0905.3390
- Milosavljević M., Phinney E. S., 2005, *ApJ*, 622, L93
- Monaghan J. J., 1992, *ARA&A*, 30, 543
- O'Neill S. M., Miller M. C., Bogdanovic T., Reynolds C. S., Schnittman J. D. 2009, *ApJ*, in press (arXiv:0812.487)
- Peres A., 1962, *Physical Review*, 128, 2471
- Price D. J., 2007, *PASA*, 24, 157
- Pringle J. E., 1991, *MNRAS*, 248, 754
- Price D. J., Monaghan J. J., 2007, *MNRAS*, 374, 1347
- Rafikov R. R., 2005, *ApJ*, 621, L69
- Rice W. K. M., Lodato G., Armitage, P. J., 2005, *MNRAS*, 364, L56
- Rodriguez C., Taylor G. B., Zavala R. T., Peck A. B., Pollack L. K., Romani R. W., 2006, *ApJ*, 646, 49
- Schnittman J. D., Krolik J. H., 2008, *ApJ*, 684, 835
- Shields G. A., Bonning E. W., 2008, *ApJ*, 682, 758
- Stone J. M., Norman M. L., 1992, *ApJS*, 80, 753
- Tichy W., Marronetti P., 2008, *Physical Review D*, 78, 081501